SUPPLEMENTARY MATERIALS

Laboratory demonstration of electron diffusive shock acceleration via pre-established ambient magnetic turbulence

X. X. Jin†,[1] Z. H. Zhao†,[1] S. K. He,[2] Z. M. Zhang,[2] X. F. Shen,[1] W. Sun,[3] L. X. Li,[1,2] Z. Lei,[1,4] Y. L. Xia,[1] D. W. Yuan,[5] Y. Dai,[6] Z. L. Ma,[7] H. H. An,[8] K. Gu,[9] H. Y. Liu,[9] N. Hua,[9] P. Z. Zhang,[9] Z. Zhang,[6] J. Y. Zhong,[7] J. Q. Zhu,[9] S. P. Zhu,[4] G. Zhao,[5] J. Zhang,[10] X. T. He,[4] W. M. Zhou*,[2] and B. Qiao*[1,11]

[1)] *Center for Applied Physics and Technology, HEDPS, and SKLNPT, School of Physics, Peking University, Beijing, China*

[2)] *Science and Technology on Plasma Physics Laboratory, Research Center of Laser Fusion, China Academy of Engineering Physics (CAEP), Mianyang, China*

[3)] *Department of Nuclear physics, China Institute of Atomic Energy, Beijing, China*

[4)] *Institute of Applied Physics and Computational Mathematics, Beijing, China*

[5)] *Key Laboratory of Optical Astronomy, National Astronomical Observatories, Chinese Academy of Sciences, Beijing, China*

[6)] *National Laboratory for Condensed Matter Physics, Institute of Physics, Chinese Academy of Sciences, Beijing, China*

[7)] *Department of Astronomy, Beijing Normal University, Beijing, China*

[8)] *Shanghai Institute of Laser Plasma, CAEP, Shanghai, China*

[9)] *National Laboratory on High Power Laser and Physics, Shanghai Institute of Optics and Fine Mechanics, Chinese Academy of Sciences, Shanghai, China*

[10)] *Key Laboratory for Laser Plasmas (Ministry of Education) and School of Physics and Astronomy, Shanghai Jiao Tong University, Shanghai, China*

[11)] *Frontiers Science Center for Nano-optoelectronic, Peking University, Beijing, China*

(Dated: 17 October 2026)

SECTION 1: BIERMMAN MAGNETIC FIELDS OF LASER-DRIVEN PLASMA FLOWS FROM PERFORATED CH FOILS

In the experiment, magnetic turbulence is generated by the collision, at the center, of two laser-driven, counter-streaming plasma flows traveling along the +y and -y directions. These plasma flows are produced by laser ablation through perforated CH foil targets. Compared with conventional planar foils, the perforated foils, which feature a 7×7 array of 60 μm-diameter holes spaced by 120 μm in the x–z plane, significantly increase the transverse density gradient ∇n_e and temperature gradient ∇T_e of the laser ablated plasmas, thereby enhancing both the strength and spatial complexity of the Biermann magnetic fields in the colliding plasma flows. Three-dimensional (3D) radiation-magnetohydrodynamic (RMHD) simulations are performed to investigate the generation of Biermann magnetic fields from laser ablated planar and perforated CH foil targets.

Figure **S1** presents the distribution maps in the x–z plane of the magnetic field components B_x [panels (b) and (g)], B_y [panels (c) and (h)] and B_z [(d) and (i)] for the two cases at time $t = 2$ ns when the laser just ends. The slices are taken along the y-direction at the location of the maximum density gradient ∇n_e, as indicated by the dashed red lines in panels (a) and (f), respectively. For the planar target, we clearly observe that B_x and B_z exhibit the characteristic topology of the Biermann magnetic field[1,2], while B_y is negligible. This is because ∇n_e is predominantly along the y-direction, while ∇T_e lies mainly in the x–z plane. The total magnetic field strength $|B_{\rm total}| = \sqrt{|B_x|^2 + |B_y|^2 + |B_z|^2}$ is about 7.5 T, as shown in panel (e).

However, for the perforated target in our experiment, we see from Fig. **S1**(f) that the ablated plasma expands much faster, with both density and temperature distributions that are spatially more complex and have larger gradients. As a result, the Biermann field $\partial B_x/\partial t = -(\nabla_z T_e \nabla_y n_e - \nabla_y T_e \nabla_z n_e)/(e n_e)$ and $\partial B_z/\partial t = -(\nabla_y T_e \nabla_x n_e - \nabla_x T_e \nabla_y n_e)/(e n_e)$ both exhibit alternating positive–negative small-scale structures, as shown in Figs. **S1**(g) and **S1**(i). Meanwhile, $\partial B_y/\partial t = -(\nabla_x T_e \nabla_z n_e - \nabla_z T_e \nabla_x n_e)/(e n_e)$ also grows rapidly, forming numerous small-scale complex structures with a strength comparable to those of B_x and B_z, as illustrated in Fig. **S1**(h). Moreover, due to the higher absorption efficiency of the perforated target and the enhanced density and temperature gradients, the total field strength of $|B_{\rm total}|$ is greatly increased to about 28 T, nearly four times that in the planar target case.

---

† These authors have contributed to this work equally.

∗ Corresponding author. e-mail:zhouwm@caep.cn,bqiao@pku.edu.cn.

Furthermore, the comparable strengths of B_x, B_y and B_z favor the subsequent development of an isotropic magnetic turbulence.

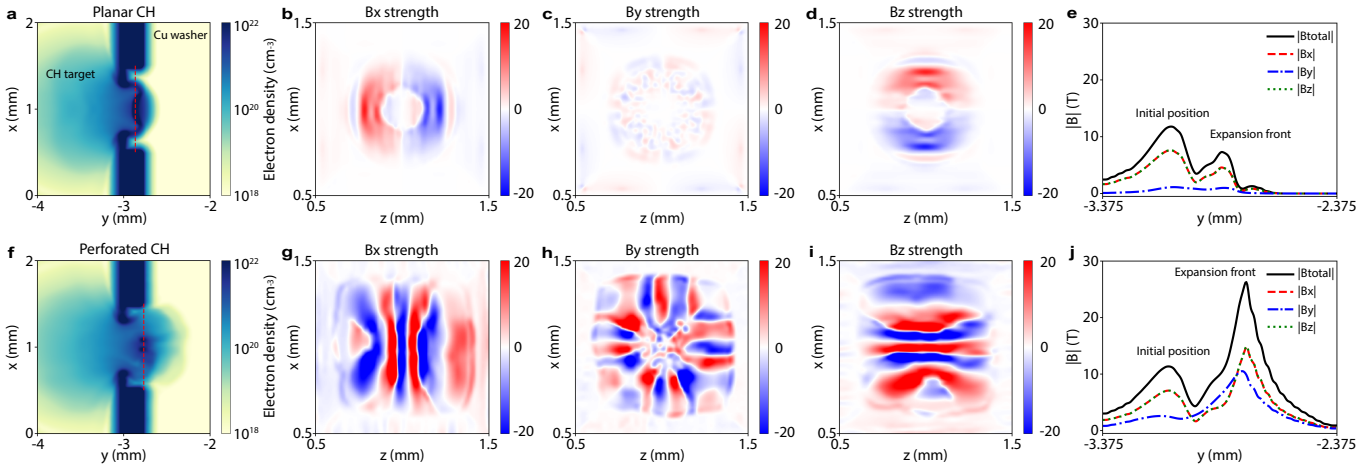


Fig S1. Three-dimensional RMHD simulation results for the generation of Biermann magnetic fields from laser ablated planar (upper row) and perforated (lower row) CH foil targets. (a)-(d) Distribution maps of density in the x–y plane cut at $z = 1$ mm and Bierman magnetic field components B_x, B_y and B_z in the x–z plane cut at the location of the maximum density gradient ∇n_e [indicated by the dashed red lines in panels (a)] for the planar target case at time $t = 2$ ns when the laser just ends. (f)-(i) are those for our perforated target case. (e) and (j) are the averaged field strength of $|B_x|$, $|B_y|$, $|B_z|$ and $|B_{\rm total}| = \sqrt{|B_x|^2 + |B_y|^2 + |B_z|^2}$ varying along the y-axis for the two cases, respectively.

SECTION 2: THE MEASURED TURBULENCE/SHOCK PLASMA DENSITIES AND TEMPERATURES

The setup of the X-ray and optical diagnostics is schematically shown in Fig. **S2**, including a time-gated X-ray detector, a time-integrated X-ray detector, optical diagnostics and a flat-field grating spectrometer. The time-gated X-ray detector records plasma self-emission images with an exposure time of 150 ps using a low-loss filter consisting of 2 μm mylar and 0.2 μm Al. The pinhole (50 μm diameter) is aligned at a 30° angle from the z-axis in the x–z plane, with a 6× magnification system projecting the 2 mm-wide plasma region onto a 12 mm-wide strip. For the optical diagnostics, an 80 ps, 527 nm probe light propagates through the plasma region and is subsequently collected by a 3× magnification imaging system. As shown in Fig. **S3**(a), the optical diagnostics consist of two channels for Nomarski interferometry and shadowgraphy, respectively, enabling measurements of electron density distributions[3,4]. A simplified Nomarski interferometer[5] is implemented, using a Wollaston prism to split the probe light into two orthogonally polarized lights that interfere after passing through the plasma. As the probe light traverses the plasma, the change in refractive index induces a phase shift relative to the reference light beam. Interference between the two light beams reveals this phase modulation, which is related to the electron density n_e through a first-order Taylor expansion of the plasma refractive index: $\Delta\phi = \frac{\omega}{2cn_c}\int n_e\, dl$, where ω is the probe light frequency and n_c is the critical density.

The formation of the collisionless shock can be identified from both optical interferometry and shadowgraphy. Figure **S3**(b) displays the interferogram recorded at 10 ns after the piston-flow-driving nanosecond laser pulses (group 2), i.e., 20 ns after the turbulence-driving nanosecond laser pulses (group 1). The interference fringes gradually shift and become increasingly distorted from right ($x = 6.5$ mm) to left, until at about $x = 4.5$ mm they disappear in a bow-shaped black region, indicating the density gradient has become so steep that the probe light can no longer penetrate the plasma. In other words, this clearly reveals a bow-shaped density discontinuity at $x = 4.5$ mm, confirming the formation of a bow-shaped collisionless shock. Furthermore, the electron density map of the shock upstream region $x \sim 5$ to 6.5 mm) reconstructed by interferometric inversion in Fig. **S3**(c) yields an upstream electron density of about (1–1.5) $\times 10^{19}$ cm^{-3} and a compressed electron density in the shock region estimated to be $> 4 \times 10^{19}$ cm^{-3}, implying a maximum density compression ratio $R = n_{\rm down}/n_{\rm up} \approx 3$. The shadowgraph image in Fig. **S3**(d) displays a consistent bow-shaped shock structure, further confirming the formation of a collisionless shock.

The properties of the pre-established magnetic turbulence are characterized with a flat-field grating spectrometer for soft X-ray emission, using a 2400 lines/mm grating. The spatially and temporally integrated plasma emission in the 1–6 nm (206–1240 eV) range is plotted in Fig. **S4**(a). Several distinct emission lines are observed superimposed on

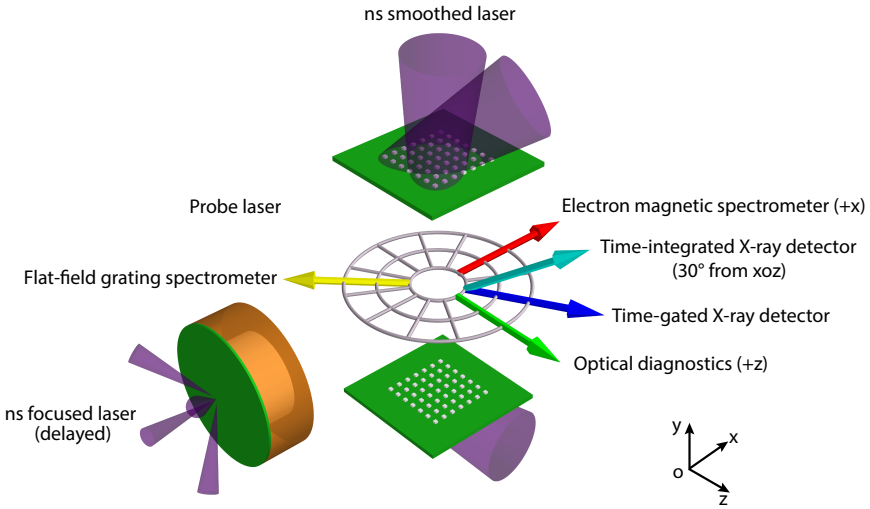


Fig S2. The setup of the X-ray and optical diagnostics of the SG-II experiments. A time-gated X-ray detector with the 150 ps gate, a time-integrated X-ray detector and the optical diagnostics are placed nearly perpendicular to the shock propagation direction to characterize the density and morphology of the turbulence and shock. A flat-field grating spectrometer is positioned in the x–z plane to measure the electron temperature of the turbulent plasma. An electron magnetic spectrometer (EMS) is positioned along the shock direction to record the electron energy spectrum.

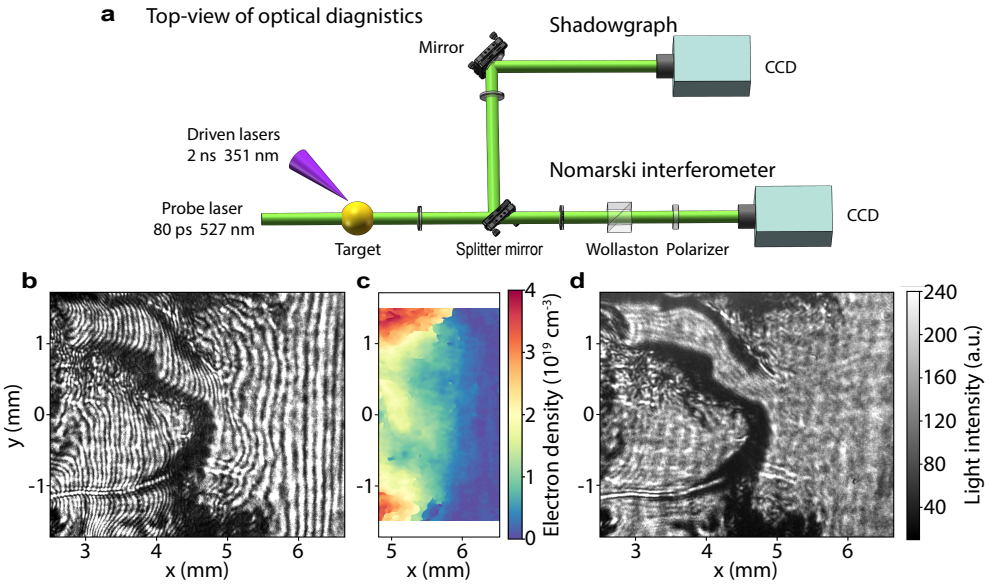


Fig S3. The optical diagnostic setup for the shock front consists of interferometry and shadowgraphy. (a) Schematic of the setup: an 80 ps, 527 nm probe pulse traverses the plasma region and is collected by a 3× magnification imaging system, which splits into two channels for Nomarski interferometry and shadowgraphy, respectively. (b) Interferogram recorded at 10 ns after the piston-flow-driving nanosecond laser pulses (group 2). (c) Electron density map of the shock upstream region ($x \sim 5$ to 6.5 mm) reconstructed by interferometric inversion. (d) Shadowgraph image of the same shot at the same time.

the bremsstrahlung continuum. The turbulent plasma electron temperature is estimated by comparing the measured line intensity ratios with FLYCHK calculations[6]. Specifically, after subtracting the bremsstrahlung background using a large-scale filter, the black line in Fig. S4(b) shows the relative intensity distribution of the measured emission lines. The peaks at 3.38 nm and 4.03 nm correspond to the Lyman-α line ($1s \rightarrow 2p$) of H-like C VI and the resonance line ($1s^2 \rightarrow 1s2p$) of He-like C V, respectively. The intensity ratio between these emission lines is about 4.2. Meanwhile, taking the electron density as 1×10^{19} cm^{-3} from the above optical interferometry, the relative intensity ratio between these two bound-bound transitions as a function of electron temperatures is calculated by the FLYCHK code, as shown in Fig. S4(c). The calculation shows that the C VI to C V intensity ratio increases

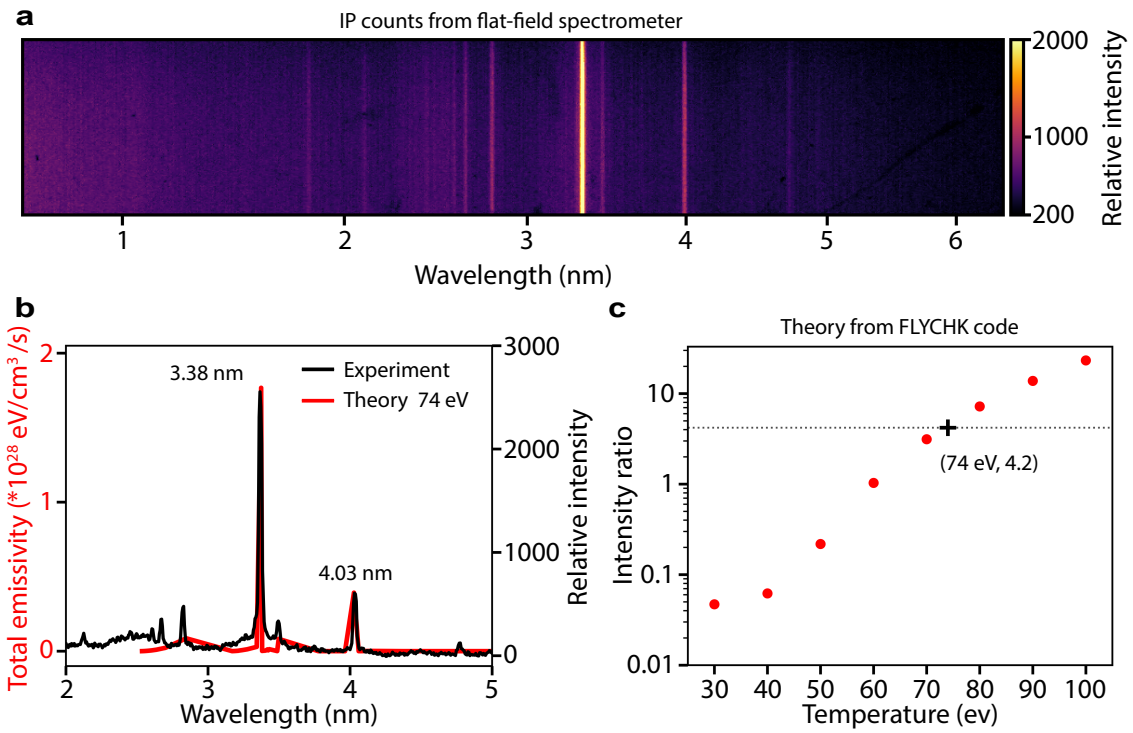


Fig S4. Soft X-ray emission from the turbulent plasma characterized with a flat-field grating spectrometer. (a) Spatially and temporally integrated plasma emission intensities in the 1-6 nm (206–1240 eV) range. (b) Relative intensity distribution of the measured emission lines in (a) after subtracting the bremsstrahlung background using a large-scale filter (black line). (c) Relative intensity ratio between the C VI and C V bound-bound transitions as a function of electron temperatures calculated with the FLYCHK code. By matching the unique correspondence, the measured ratio of 4.2 yields a plasma electron temperature of 74 eV via linear interpolation, as marked by the black cross in (c). The red line in (b) is the total emission spectrum of the carbon plasma at 74 eV calculated by the FLYCHK code.

monotonically with plasma electron temperatures. By matching the unique correspondence, the plasma electron temperature corresponding to the measured ratio of 4.2 is determined to be 74 eV via linear interpolation (marked by the black cross). For validation, the total emission spectrum of the carbon plasma at 74 eV calculated by FLYCHK is plotted as the red line in Fig. **S4**(b), which is in good agreement with the experimental measurement (black line).

SECTION 3: TURBULENCE SCATTERING AND DIFFUSION PROPERTIES FOR ELECTRONS

To achieve DSA, shocks alone are insufficient; turbulence on both sides of the shock is equally essential. On the one hand, turbulence scatters electrons that would otherwise escape after a single shock crossing, redirecting them back into the acceleration cycle and enabling further energy gain. On the other hand, turbulence promotes isotropization in the local wave frame, preserving the balance between the energy-gain probability per cycle and the escape probability[7], without which the power-law spectrum would break down. While downstream turbulence arises naturally from the strong dissipation of the shock itself[8], upstream turbulence generally requires sustained instability growth like Bell instability in high-Mach-number shocks[9], or pre-existing magnetic turbulence[10,11].

The distribution function $f(t, x, p)$ of particles accelerated via DSA can be described by the diffusion–convection equation (the Parker transport equation) in the fluid rest frame[12–14]:

$$\frac{\partial f}{\partial t} = -u\frac{\partial f}{\partial x} + \frac{\partial}{\partial x}\left[\overline{D}(x,p)\frac{\partial f}{\partial x}\right] + \frac{p}{3}\frac{du}{dx}\frac{\partial f}{\partial p},$$

where the three terms on the right-hand side represent convection, diffusion, and adiabatic compression, respectively, and together drive particle acceleration. The quasi-steady diffusion coefficient $\overline{D}(x, p)$ depends on the magnetic field irregularities in both upstream and downstream turbulence, including both its fluctuating and mean components, and thus encapsulates the wave-particle interactions that govern the spatial random walk of particles along the gradient

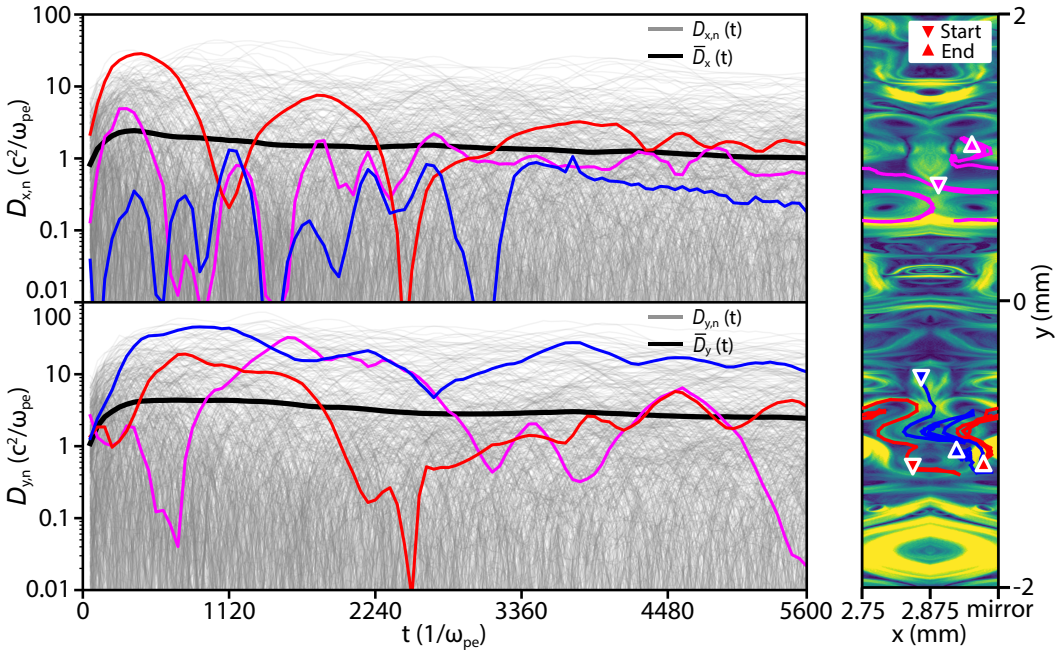


Fig S5. The diffusion coefficient for the turbulence in the region of $x \in [2.75, 2.875]$ mm near the shock front obtained using the test particle simulations [corresponding to the green triangular data point in Fig. 3(f) of the main manuscript]. The turbulent magnetic field is extracted directly from the PIC simulation at $t = 22$ ns and mirrored along the x-direction for another 0.125 mm, as shown in right panel. In the left panel, the grey curves show the time-dependent diffusion coefficients $D_{x,n}(t)$ (upper half) and $D_{y,n}(t)$ (lower half) for all tracked electrons, while the bold black lines represent the corresponding averages $\overline{D}_x(t)$ and $\overline{D}_y(t)$. Three representative electron trajectories and their diffusion coefficients are highlighted in red, purple and blue.

of f[14]. In the weak turbulence with a uniform background magnetic field, the diffusion coefficient is generally approximated by the Bohm diffusion $\overline{D}(p) \approx r_{ce} v_e$, where r_{ce} and v_e denote the gyroradius and velocity of the electron.

However, in the quasi-isotropic strong turbulence realized in our experiments, the dependence of the diffusion coefficient $\overline{D}(x, p)$ on the turbulent magnetic field is not yet understood theoretically, as its specific value varies with spatial position x and particle momentum p. Therefore, we perform a large number of small-scale test-particle simulations to obtain the local diffusion coefficient $\overline{D}(x, p)$ by statistically averaging over a small-scale spatial domain and taking the asymptotic steady value, where the local turbulent magnetic fields are extracted directly from the PIC simulations in the manuscript [Figs. 3(a) and 3(d)]. This method has been previously adopted and validated[15,16].

Here, we primarily study the turbulence diffusion properties in a region of width 1.75 mm near the shock front: $x \in [0.625, 2.375]$ mm at $t = 19$ ns (blue) and $x \in [1.875, 3.625]$ mm at $t = 22$ ns (red), as shown in Fig. 3(f) of the main manuscript. To obtain the local diffusion coefficient $\overline{D}(x, p)$ at different positions such as 14 blue plus 14 red points in Fig. 3(f), we have performed 28 test-particle simulations, each within a small domain of size 0.125 mm (= 1.75/14 mm). To characterize the local diffusion properties while excluding other effects, we require magnetic field continuity and periodic boundaries in the x-direction; therefore, each simulation domain is mirrored along the x-direction by an additional 0.125 mm width.

Test electrons of various energies are uniformly initialized within the simulation domain, where their momentum directions are randomly oriented in three dimensions. These electrons then undergo diffusive motion in the local turbulent magnetic field. The time-dependent diffusion coefficient $\overline{D}_x(t)$ for electrons of energy E in the x-direction is evaluated as

$$\overline{D}_x(t) \equiv \frac{1}{N} \sum_{n=1}^{N} D_{x,n}(t) = \frac{1}{2tN} \sum_{n=1}^{N} |x_n(t) - x_n(0)|^2 , \tag{1}$$

where N is the total number of tracked particles, and $x_n(t)$ is the x coordinate of an individual particle n at time t. The quantity $\overline{D}_y(t)$ can be evaluated analogously. Under strong turbulent scattering, $\overline{D}_x(t)$ converges to a steady value over time, i.e., $\overline{D}_x = \lim_{t\to\infty} \overline{D}_x(t)$.

As an example, we present one test-particle simulation used to obtain the green triangle data point in Fig. 3(f) of the main manuscript. The domain is chosen as $x \in [2.75, 2.875]$ mm near the shock front, and the turbulent magnetic

field is extracted directly from the PIC simulation at $t = 22$ ns, as shown in the right panel of Fig. S5. More than 10^5 test electrons with initial energies of 210 keV (the injection energy inferred from the experiments) are uniformly initialized in a 0.25×4 mm^2 simulation domain. We randomly select 500 test electrons and track their motion, recording trajectories every 100 time steps. For each tracked particle, the time-dependent diffusion behavior in the x and y directions is calculated independently.

The grey curves in the left panel of Fig. S5 show the obtained time-dependent diffusion coefficients $D_{x,n}(t)$ (upper half) and $D_{y,n}(t)$ (lower half) for all tracked electrons, and the bold black lines represent the corresponding averages $\overline{D}_x(t)$ and $\overline{D}_y(t)$. Although the individual particle behaviors appear somewhat random and erratic, the averaged diffusion coefficients converge to well-defined asymptotic limits: $\overline{D}_x = \lim_{t\to\infty} \overline{D}_x(t) \approx 1.02\ c^2/\omega_{pe}$ and $\overline{D}_y = \lim_{t\to\infty} \overline{D}_y(t) \approx 2.44\ c^2/\omega_{pe}$, confirming the diffusive nature of transport near the shock front. Three representative electron trajectories and their diffusion coefficients are highlighted in red, purple and blue, illustrating how the diffusion coefficient of an individual electron reaches its asymptotic value.

In the same manner, we use a series of test-particle simulations to obtain the diffusion coefficients at the remaining positions near the shock, marked by other 27 data points in Fig. 3(f) of the main manuscript.

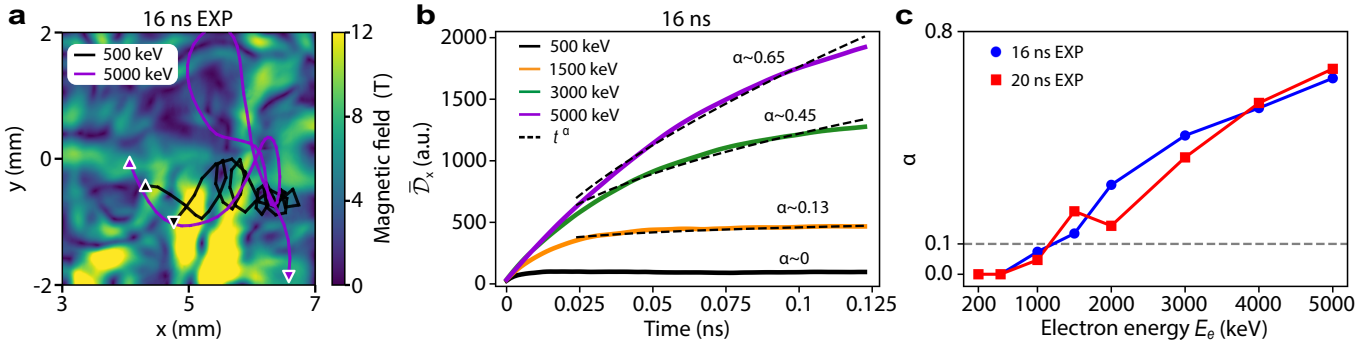


Fig S6. Electron diffusion analysis via test-particle simulations in magnetic fields directly reconstructed from proton radiography. (a) Magnetic field distribution at $t = 16$ ns reconstructed from experimental proton radiography [Figs. 1(b) and 1(c)], which serves as the input for test-particle simulations. The black and purple lines display the simulated trajectories of electrons with energies of 500 keV and 5000 keV, respectively. (b) Equivalent diffusion coefficient $\overline{\mathfrak{D}}$ as a function of time for test electrons with initial energies ranging from 500 to 5000 keV. (c) Fitted asymptotic exponent α as a function of electron initial energy for the turbulent magnetic fields at $t = 16$ ns and $t = 20$ ns.

Since proton radiography in experiments only provides the two-dimensional topology of magnetic fields $B_{xy} = \sqrt{B_x^2 + B_y^2}$ without any information on B_z, and its spatial resolution is rather limited, it is impossible to accurately calculate the diffusion coefficient $\overline{D}_x(t)$ directly from the experimental data. We therefore only illustrate the diffusion transport characteristics of the measured turbulent magnetic field at $t = 16$ ns [Figs. 1(b) and 1(c)] using test-particle simulations. In these simulations, the specific magnetic field strength distribution, shown in Fig. S6(a), is constructed from the relative values of the magnetic field path-integrated distribution in Figs. 1(b) and 1(c), assuming a path length $l_{\rm path} \approx 1$ mm and taking the root-mean-square magnetic field as $B_{\rm rms} \approx 8.1$ T (as estimated in the main manuscript). Similarly, through test-particle simulations, we can also give a rough evaluation of the equivalent diffusion coefficient as a function of time: $\overline{\mathfrak{D}} \propto \sum_{n=1}^{N} |x_n(t) - x_n(0)|^2 / (2tN) \propto t^\alpha$, where α is an index. When particles experience sufficient pitch-angle scattering in the turbulent magnetic field, their motion resembles a random walk; the particle mean displacement stays near zero while the mean square displacement grows linearly with time, i.e. $|x_n(t) - x_n(0)|^2 \propto t$. Consequently, in the diffusive limit, $\overline{\mathfrak{D}} \propto t^0$ ($\alpha = 0$). On the other hand, when the pitch-angle scattering is insufficient, the particle motion is instead dominated by their free-streaming velocity v, giving $|x_n(t) - x_n(0)|^2 \propto v^2 t^2$, and hence $\overline{\mathfrak{D}} \propto t^1$ ($\alpha = 1$).

The resulting equivalent diffusion coefficient $\overline{\mathfrak{D}}$ as a function of time for test electrons with different initial energies from 200 to 5000 keV is shown in Fig. S6(b). For electrons with a moderate energy of 500 keV, $\overline{\mathfrak{D}}$ approaches an asymptotic limit corresponding to $\alpha = 0$, indicating a well-defined diffusion process. The electron trajectory [black line in Fig. S6(a)] further confirms this diffusive behavior: the electron undergoes frequent reflections and scattering within the magnetic turbulence. As the initial energy increases, $\overline{\mathfrak{D}}$ gradually transitions from diffusion-dominated to streaming-dominated motion, with α rising up to 0.65 at 5000 keV. This transition is also corroborated by the large-scale Larmor gyration evident in the electron trajectory [purple line in Fig. S6(a)].

We have applied the same test-particle analysis to the magnetic field at $t = 20$ ns [Figs. 1(d) and 1(e)]. The fitted asymptotic values of α for electrons with different initial energies are plotted in Fig. S6(c) (red line with dots),

alongside the results for the $t = 16$ ns case (blue line with dots). It is clearly seen that the turbulent magnetic fields at both times efficiently drive diffusive transport for electrons with energies around 500 keV ($\alpha = 0$), while this confining ability gradually weakens with increasing energy. This behavior is consistent with the energy spectra measured in our experiments, which exhibit a cutoff at ~ 500 keV, directly confirming that the turbulence-mediated shock in the present experiment is capable of accelerating electrons via DSA up to 500 keV. In the future, with higher laser energy, DSA of electrons towards MeV energies may become achievable.

REFERENCES

[1]Stamper, J. A. et al. Spontaneous magnetic fields in laser-produced plasmas. *Phys. Rev. Lett.* **26**, 1012–1015 (1971).
[2]Schoeffler, K. M. et al. Magnetic-field generation and amplification in an expanding plasma. *Phys. Rev. Lett.* **112**, 175001 (2014).
[3]Ping, Y. L. et al. Turbulent magnetic reconnection generated by intense lasers. *Nat. Phys.* **19**, 263–270 (2023).
[4]Yuan, D. et al. Electron stochastic acceleration in laboratory-produced kinetic turbulent plasmas. *Nat. Commun.* **15**, 5897 (2024).
[5]Hough, P. et al. Time resolved Nomarski interferometery of laser produced plasma plumes. *Appl. Surf. Sci.* **255**, 5167–5171 (2009).
[6]Lee, R. W. & Larsen, J. T. A time-dependent model for plasma spectroscopy of K-shell emitters. *J. Quant. Spectrosc. Radiat. Transfer* **56**, 535–556 (1996).
[7]Bell, A. R. The acceleration of cosmic rays in shock fronts. I. *Mon. Not. R. Astron. Soc.* **182**, 147–156 (1978).
[8]Giacalone, J. & Jokipii, J. R. Large-scale turbulence, shocks, and charged-particle acceleration. *AIP Conf. Proc.* **932**, 243–257 (2007).
[9]Bell, A. R. Turbulent amplification of magnetic field and diffusive shock acceleration of cosmic rays. *Mon. Not. R. Astron. Soc.* **353**, 550–558 (2004).
[10]Treumann, R. A. Fundamentals of collisionless shocks for astrophysical application, 1. Non-relativistic shocks. *Astron. Astrophys. Rev.* **17**, 409–535 (2009).
[11]Perri, S. et al. Recent developments in particle acceleration at shocks: theory and observations. *Space Sci. Rev.* **218**, 26 (2022).
[12]Drury, L. O'C. An introduction to the theory of diffusive shock acceleration of energetic particles in tenuous plasmas. *Rep. Prog. Phys.* **46**, 973–1027 (1983).
[13]Parker, E. N. The passage of energetic charged particles through interplanetary space. *Planet. Space Sci.* **13**, 9–49 (1965).
[14]Guo, F., Giacalone, J. & Zhao, L. Shock Propagation and Associated Particle Acceleration in the Presence of Ambient Solar-Wind Turbulence. *Front. Astron. Space Sci.* **8**, 644354 (2021).
[15]Caprioli, D. & Spitkovsky, A. Simulations of ion acceleration at non-relativistic shocks. III. Particle diffusion. *Astrophys. J.* **794**, 47 (2014).
[16]Gupta, S., Caprioli, D. & Spitkovsky, A. Speed-dependent threshold for electron injection into diffusive shock acceleration. *Astrophys. J. Lett.* **994**, L34 (2025).